Acta Oceanol. Sin., 2017, Vol. 36, No. 7, P. 86–94
DOI: 10.1007/s13131-017-1086-z
http://www.hyxb.org.cn
E-mail: hyxbe@263.net

A novel oil spill detection method from synthetic aperture radar imageries via a bidimensional empirical mode decomposition

YANG Yonghu[1, 2], LI Ying[1]*, ZHU Xueyuan[1]

[1] Navigation College, Dalian Maritime University, Dalian 116026, China

[2] Computer Science and Technology Department, Dalian Neusoft Institute of Information, Dalian 116023, China

Received 15 June 2016; accepted 5 July 2016

Abstract

Oil spills pose a major threat to ocean ecosystems and their health. Synthetic aperture radar (SAR) sensors can detect oil spills on the sea surface. These oil spills appear as dark spots in SAR images. However, dark formations can be caused by a number of phenomena. It is aimed to distinguishing oil spills or look-alike objects. A novel method based on a bidimensional empirical mode decomposition is proposed. The selected dark formations are first decomposed into several bidimensional intrinsic mode functions and the residue. Subsequently, 64 dimension feature sets are calculated using the Hilbert spectral analysis and five new features are extracted with a relief algorithm. Mahalanobis distances are then used for classification. Three data sets containing oil spills or look-alikes are used to test the accuracy rate of the method. The accuracy rate is more than 90%. The experimental results demonstrate that the novel method can detect oil spills validly and accurately.

Key words: bidimensional empirical mode decomposition, synthetic aperture radar image, detection of oil spill, hilbert spectral analysis

Citation: Yang Yonghu, Li Ying, Zhu Xueyuan. 2017. A novel oil spill detection method from synthetic aperture radar imageries via a bidimensional empirical mode decomposition. Acta Oceanologica Sinica, 36(7): 86–94, doi: 10.1007/s13131-017-1086-z

1 Introduction

The sea area accounts for approximately 71% of the earth. The sea is the most stable ecosystem on the planet. It has vast space and rich resources and plays a significant role in the global ecological environment regulation. With the development of industries worldwide, sea pollution is becoming increasingly serious. At present, sea pollution includes oil pollution, red tide, toxic substances, plastic pollution, and nuclear contamination. Oil pollution, which originates mostly from accidental and deliberate discharges into the ocean of hydrocarbon products from large ships/tankers and oil platforms, constitutes the predominant portion of sea pollution. However, ship and oil-rig accidents, such as the Prestige disaster in 2002 off the west coast of Spain and the more recent Deepwater Horizon well blowout in 2010 in the Gulf of Mexico, exert a considerable effect on the ecology and wildlife of the polluted area. Chronic illegal releases of oil from ships and offshore platform operations are extremely frequent along the main shipping route and over zones of offshore oil extraction structures (Brekke and Solberg, 2005; Zheng et al., 2010). The accurate detection and forecast of oil spill trajectory would be beneficial to fisheries, wildlife, and resource management for the monitoring and conservation of the marine environment. The detection and forecast are some of the most important applications for operational oceanography (Cheng et al., 2011).

The monitoring and detection of oil spills by using synthetic aperture radar (SAR) systems have received considerable attention over the past few years because of their wide area coverage and day and night capabilities. Several space-borne SAR systems are used for oil spill monitoring, including the SAR systems, which were launched by the Russian Space Agency, the European Space Agency, and the Canadian Space Agency (Topouzelis, 2008). A scan SAR narrow mode can monitor the Gulf of Mexico oil disaster (Marghany, 2015). Bern et al. (1993) monitored oil spill using ERS data. Pavlakis et al. (1996) monitored an oil spill accident happened in the Mediterranean Sea using the ERS data. Nunziata et al. (2011) employed fully polarimetric SAR measurements for a sea oil slick observation. However, at wind speeds below 2–3 m/s, a backscatter cannot be observed from the sea surface; hence, the signature of oil slicks is absent. Ideal conditions for the SAR imaging of oil slicks could be wind speeds between 3 and 10 m/s (Solberg, 2012). In addition, oil slicks dampen the Bragg waves on the ocean surface and reduce the radar backscatter coefficient, resulting in dark regions or spots in a SAR image. The complexity of the marine system radar detection of oil spills is highly susceptible to false detections or look-alikes, including natural films/slicks, grease ice, threshold wind speed areas, wind sheltering by land, rain cells, shear zones, and internal waves (Brekke and Solberg, 2005). The differences between oil spills and quasi-oil spills reflected in the SAR image exist. For example, the low wind speed region has several characteristics of larger area, irregular shape, and vague edges generally. Internal waves manifests itself on the radar image as the alternate stripes of bright and dark. Ship wakes tend to be V-shaped lines or strip lines in the SAR images. The efficiency of manual monitoring is low. Thus, this detection poses a fundamental challenge in discriminating between oil spills and look-

Foundation item: The National Science and Technology Support Project under contract No. 2014BAB12B02; the Natural Science Foundation of Liaoning Province under contract No. 201602042.
*Corresponding author, E-mail: yldmu@126.com

alikes by an automatic method. In recent years, numerous approaches have been developed and tested to distinguish oil spills from other similar oceanic features in the marine SAR images (Nirchio et al., 2005). In general, the detection of oil spill from the SAR imagery includes two steps: image preprocessing and oil spill identification. The preprocessing can provide the regions of interest (ROIs) for identification by segmenting the SAR images. The second step mainly identifies between oil spills and lookalikes by extracting features and using several classification algorithms.

The main purpose of the preprocessing phase is to segment the SAR image that subdivides an image into its constituent parts and extracts dark regions. Image segmentation approaches are currently based on detecting discontinuities and similarities (Chaudhuri et al., 2012). These approaches include image segmentation algorithms, such as edge detection, thresholding, region growing, clustering, and neural networks. In this study, this step uses a histogram to obtain the ROI.

In the oil spill identification phase, several researchers detect oil spills from look-alikes by using multi features. Most published papers discuss features, such as texture features, gray features, and physical characteristics. Frate et al. (2000) considered the extension and shape of the dark object and used 11 geometrical characteristics. Zhang et al. (2008) extracted five textural features based on a co-occurrence matrix. Salberg et al. (2014) described several physical mechanism features of the backscatter. Guo and Zhang (2014) analyzed the importance of individual features and selected nine shape features. Chaudhuri et al. (2012) presented a statistical-based approach to detect the dark curvilinear features. Stine Skrunes et al. (2014) extracted two multi-polarization features that can be used to distinguish between the simulated biogenic slicks and mineral oil types. However, feature extraction and applications by using decomposition technologies, such as Fourier and wavelet decomposition, are rarely discussed because basic functions are fixed in these approaches and do not necessarily match the varying nature of signals. Fourier transform can introduce false harmonic components that can cause the spread of the energy. Wavelet decomposition results largely depend on the selection of a wavelet basis function, so adaptability is weak. An empirical mode decomposition (EMD), as a new technology of a time frequency analysis, has multi scale and multi resolution characteristics. It is a process of constant loop iteration and is suited to solve the problem of nonlinear and non-stationary systems. It is applied to texture segmentation by analyzing the instantaneous frequency of the obtained components called intrinsic mode functions (IMFs) (Liu and Peng, 2005; Chen et al., 2012). Dong et al. (2010) used the EMD to extract several IMF energy features, such as inputted parameter of neural networks, to classify oil slicks and sea water. Nunes et al. (2003) developed an algorithm based on the bidimensional EMD (BEMD) to extract features at multiple scales or spatial frequencies. Nunes et al. (2005) applied the Hilbert-Huang transform and the BEMD for a texture analysis. Chen et al. (2012) combined a BEMD with a local binary pattern for a texture image classification. He et al. (2013) proposed a hyper spectral image classification method based on an improved BEMD. Chen et al. (2014) proposed a novel infrared small target detection method based on the BEMD. The present study proposes an oil spill detection method from the SAR imagery based on the BEMD. The framework for oil spill and look-alike classification based on the BEMD method is show in Fig. 1.

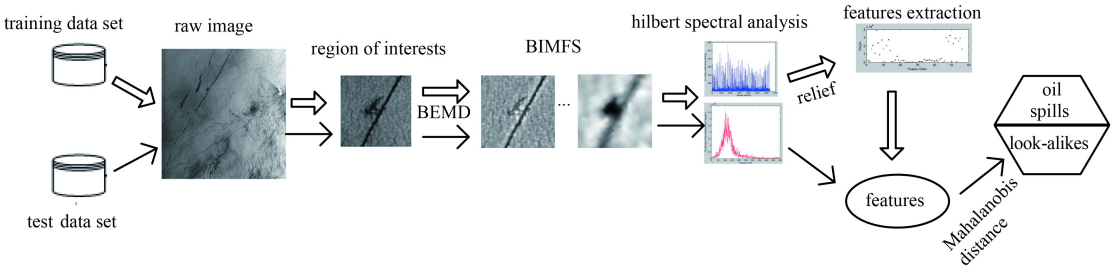

Fig. 1. The framework diagram of our proposed method.

2 Data set

Four research institutions, namely, the University of Hamburg, the Russian Academy of Sciences, the National University of Singapore, and the National Central University, cooperated and competed on a project named "the tropical and subtropical ocean viewed by ERS SAR". These institutions created a website to attract the attention of a broad readership in countries that lie in tropical and subtropical zones to the ERS SAR imagery acquired over the oceans and to motivate scientists from these countries to use the images for oceanographic and meteorological investigations (http://www.ifm.zmaw.de/fileadmin/files/ers-sar/index.html). These institutions assembled 180 sample ERS SAR images acquired over tropical and subtropical ocean areas that show typical sea surface manifestations of several oceanic and atmospheric phenomena. The oceanic phenomena that can be delineated on the SAR images of the sea surface include ocean surface waves, internal waves, eddies, oceanic fronts, underwater bottom topography, ship wakes, oceanic wakes behind islands, oil slicks, river plumes, and upwelling areas. The atmospheric phenomena include katabatic wind fields, land-sea breeze, atmospheric wakes behind islands and coastal mountains, gap winds, boundary layer rolls, convective cells, atmospheric gravity (or internal) waves, and rain cells. The data set contains several sea states, and all images contain a certain number of dark objects. These images are used to test the quality of our method. The samples of the images are shown in Figs 2 and 3.

The SAR aboard European remote-sensing satellites ERS-1 and ERS-2, which were launched in 1991 and 1995, respectively, provide the images of the earth's surface with a resolution of 25 m. In the so-called "image mode", the SAR images are taken along a 100 km wide swath to the right of the satellite track. The SARs aboard the two satellites possess identical designs. They operate at a frequency of 5.3 GHz, transmit and receive the radar signal at vertical polarization (VV polarization), and view the earth's surface under an incidence angle centered at approximately 23°. In Fig. 2, the bright area in the image is caused by an

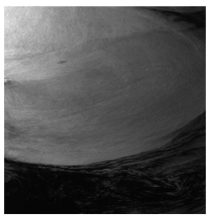

Image data	Gulf of Tehuantepec
Date	14 Mar. 1996
Time	04: 52
Orbit	04697
Frame	0279-0297
Satellite	ERS-2
Latitude	14°51′N
Longitude	95°14′W
Size	800×844

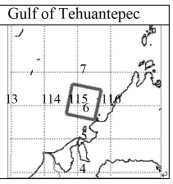

Fig. 2. ERS2 SAR image of Pacific Mexican coast.

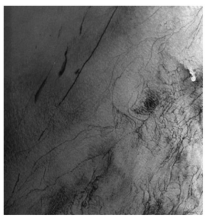

Image data	Gulf of Tehuantepec
Date	13 Jul. 1997
Time	02: 42
Orbit	11652
Frame	3483
Satellite	ERS-2
Latitude	6°07′N
Longitude	115°12′E
Size	800×844

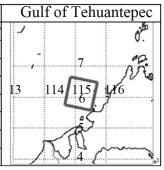

Fig. 3. ERS-2 SAR image of a sea area in the South China Sea off the west coast of Sabah (Borneo).

anticyclonic warm eddy in the Gulf of Tehuantepec, which is located on the Pacific coast of Mexico. In this location, the water temperature is several degrees Celsius higher than that in the surrounding area (black area in the image). These eddies, which typically possess a diameter of approximately 200 km, are generated by strong winds that originate in the Gulf of Mexico and blow through a narrow gap in the mountain range in the Isthmus of Tehuantepec onto the eastern tropical Pacific Ocean. The dark streaks that are visible in the left-hand section in Fig. 3 result from the oil discharge from ships. In one case, the ship (white spot) is visible at the front of the oil trail. The dark streaky features that are visible in the right-hand section of the image could originate from oil seeps.

3 Methods

3.1 *Region of interests*

A typical histogram of dark formations generally contains two peaks. The lower peak is located around the mean backscattering value of the dark object, whereas the higher peak is around the mean value of the background. Therefore, the subimages with twin peaks are the ROIs. To identify the existence of the two peaks, we need to set a threshold value, which is a static value based on several experiments and expert experience. The algorithm is described as follows:

Step 1. Read SAR image.

Step 2. A sliding window (5×5) is applied to locating salient points, which are selected as seed points. Considering processing speed and effect, ROIs (80×80) are extracted by a diffusion growth, such that areas of interest would be in the center of the window.

Step 3. Obtain the gray histogram of each subimage, that is, ROIs.

Step 4. Assess whether the histogram presents a bimodal pattern or otherwise. Supposing the peak is one point greater than its neighbor points (left, right), find the gray values of these peaks and obtain the peak point of the maximum gray value. Search the adjacent peak to the maximum peak through iteration. When the gray level difference is greater than a certain threshold value, that is 30, then stop the algorithm. The value is obtained by experience and many experiments.

Step 5. Save subimages to files, as shown in Fig. 4.

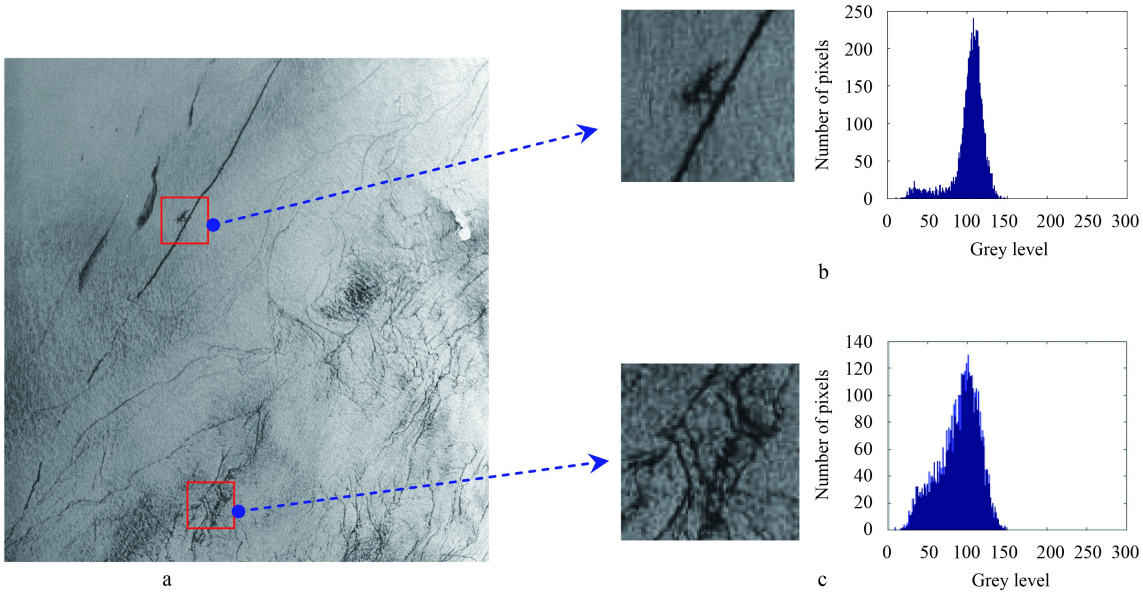

Fig. 4. Two regions of interest of Fig. 3 by our proposed method. a. Original image, b. oil spill subimage and its histogram, and c. look-alike subimage and its histogram.

3.2 *BEMD*

3.2.1 *Overview*

The EMD is proposed for processing of nonstationary and nonlinear signals, such as radar signal. Its principle involves decomposing a signal into its IMFs and a residue signal. Each IMF includes the same number of extrema and number of zero crossings. Each IMF is symmetric about the time axis with respect to the local mean. BEMD is the extension of the EMD from 1-D to 2-D data. The BEMD promotes the applications of the EMD in a 2-

D signal, such as image processing.

The BEMD decomposes an image into its bidimensional IMFs (BIMFs) and a residue signal. The difference is that the curve fitting of the maxima and minima envelope now becomes a surface fitting exercise, and the identification of the local extrema is performed in space to consider the connectivity of the points (Nunes et al., 2003). The given image can be expressed as Eq. (1) by the sum of several BIMF (f_{bim}) components and the residue:

$$I(x,y)=\sum_{i=1}^{N} f_{\text{bim},i}(x,y)+R(x,y), \tag{1}$$

where N is the number of the BIMF components and $R(x,y)$ denotes the residuary component.

The main steps of the BEMD can be described as follows:

Step 1. Initialization: i=1, d_0=$I(x,y)$, $R_0(x,y)=I(x,y)$.

Step 2. Obtain the local maximum gray value $[E_{\max}(x,y)]$ and minimal gray value $[E_{\min}(x,y)]$ of an image.

Step 3. Construct maxima and minima envelope curve surfaces $[S_{\max}(x,y)$ and $E_{\min}(x,y)]$ by using trigonometric interpolation or radial basis function. The former is faster to compute and applied in this paper.

Step 4. Compute the mean envelope curve surface $[S_{\text{m}}(x,y)]$.

Step 5. Set $d_i(x,y)=d_{i-1}(x,y)-S_{\text{m}}(x,y)$.

Step 6. Check whether $d_i(x,y)$ satisfies the BIMF properties by finding the standard deviation, denoted as (SD, d_{s}). Usually, $d_i(x,y)$ is a BIMF if the SD is greater than 0.3 (Nunes et al., 2005). If the SD is less than 0.3, then $f_{\text{bim},i}(x,y)=d_i(x,y)$. Otherwise, repeat Steps 2 to 6.

$$d_{\text{s}}=\sum_{x=0}^{M}\sum_{y=0}^{N}\left[\frac{|d_{i-1}(x,y)-d_i(x,y)|}{d_{i-1}^2(x,y)}\right]. \tag{2}$$

Step 7. Take the residual as the original image and go to Step 1 to create the next BIMF until we obtain sufficient BIMFs.

3.2.2 *Experiment*

Decomposition in Figs 4b and c is performed in three modes with the stopping criteria of the standard deviation being 0.3. The three BIMFs and their corresponding residues of the image are shown in Fig. 5.

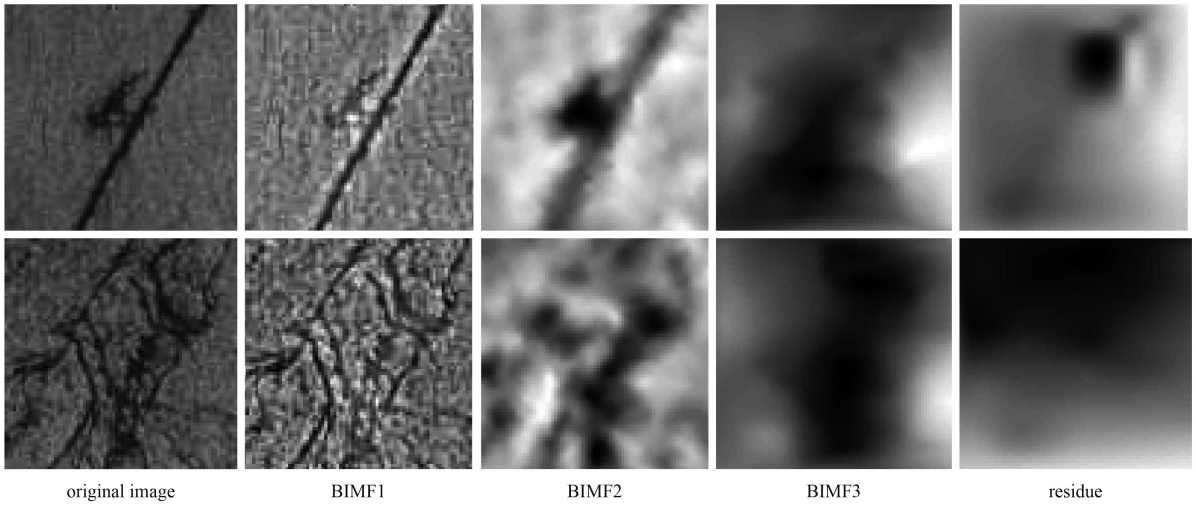

Fig. 5. BIMFs of Figs 4b and c.

3.3 *Hilbert spectral analysis*

3.3.1 *Overview*

As previously discussed, the BEMD can generate predominantly monocomponent BIMFs. The Hilbert transform can be applied to each BIMF component and compute instantaneous frequency and amplitude. Most of the studies show that the Hilbert spectrum can be derived from the IMF of the EMD, whose input is a 1-D array. However, the BIMF of the BEMD is a 2-D array. If the Hilbert spectrum can be obtained by the Hilbert transform, the input should be initially converted to the 1-D array. The method of conversion is as follows:

The matrix ($\boldsymbol{M}$) size of one BIMF component is n×m,

$$\boldsymbol{M}=\begin{pmatrix} x_{11}\cdots x_{1m} \\ \vdots \quad\quad \vdots \\ x_{n1}\cdots x_{nm} \end{pmatrix}. \tag{3}$$

$\boldsymbol{M}$ is converted to a 1-D array $\boldsymbol{X}$.

$$\boldsymbol{X}=\begin{pmatrix} x_{11},x_{12},\ldots,x_{1m},x_{21},x_{22},\ldots,x_{2m}, \\ \ldots,x_{n1},x_{n2},\ldots,x_{nm} \end{pmatrix}. \tag{4}$$

For a BIMF series $\boldsymbol{X}_i(t)$ $(t=n\times m)$, the Hilbert transform $\boldsymbol{Y}_i(t)$ can be described as

$$\boldsymbol{Y}_i(t)=\frac{1}{\pi}P\int_{-\infty}^{+\infty}\frac{\boldsymbol{X}_i(t')}{t-t'}\mathrm{d}t', \tag{5}$$

where P is the Cauchy principal value and $\boldsymbol{X}_i(t)$ and $\boldsymbol{Y}_i(t)$ form the complex conjugate pair; the analytic signal $\boldsymbol{Z}_i(t)$ is given by

$$\boldsymbol{Z}_i(t)=\boldsymbol{X}_i(t)+j\boldsymbol{Y}_i(t)=a_i(t)e^{j\theta(t)}, \tag{6}$$

where the amplitude $a_i(t)$ and the phase $\theta_i(t)$ are determined by

$$\begin{aligned} a_i(t)&=\sqrt{\boldsymbol{X}_i^2(t)+\boldsymbol{Y}_i^2(t)}, \\ \theta_i(t)&=\arctan\left(\frac{\boldsymbol{Y}_i(t)}{\boldsymbol{X}_i(t)}\right). \end{aligned} \tag{7}$$

If the signal $\boldsymbol{X}_i(t)$ is monocomponent, then the instantaneous frequency $\omega_i(t)$ can be given as

$$\omega_i(t) = \frac{\mathrm{d}\theta_i(t)}{\mathrm{d}t}. \tag{8}$$

The Hilbert spectrum is defined as

$$\begin{aligned} H(\omega, t) &= \mathrm{Re}\sum_{i=1}^{N} a_i(t)\mathrm{e}^{j\theta_i(t)} \\ &= \mathrm{Re}\sum_{i=1}^{N} a_i(t)\mathrm{e}^{j\int \omega_i(t)\mathrm{d}t}, \end{aligned} \tag{9}$$

where Re is the real part of the term.

Therefore, the Hilbert instantaneous energy E_i can be defined as

$$E_\mathrm{i} = \int_0^T H^2(\omega, t)\mathrm{d}t. \tag{10}$$

The entropy S of the instantaneous frequency for a given frame is defined as Eq. (11):

$$S = \int_w H^2(\omega, t)\mathrm{d}w. \tag{11}$$

In summary, the HSA can compute instantaneous frequency and amplitude, and can consequently construct a 3-D time frequency diagram. The marginal spectrum that represents the accumulated amplitude (energy) over the entire data can be also acquired.

3.3.2 *Experiment*

For the first BIMF of Figs 4b and c, the instantaneous frequencies are respectively computed. After normalization processing, the Hilbert instantaneous energy and the entropy of the instantaneous frequency can be obtained based on the above definition. Their three diagrams are shown in Figs 6 and 7.

3.4 *Feature extraction*

Each ROI image is decomposed into three IMFs and the residual by the BEMD. The 2-D data are then transformed into the 1-D data to calculate the Hilbert spectrum and the Hilbert marginal spectrum. Afterward, the amplitude and frequency information can be easily extracted. A feature vector should be constructed to perform a good texture analysis. In this work, several new feature parameters were designed to discriminate oil spills from look-alikes. These values create the 16-dimensional pixel feature vectors of the first IMF. This step was performed for all IMFs and the residue. Therefore, the feature vectors are generated for each ROI as Eq.(12):

$$\begin{aligned} \bar{\boldsymbol{T}} &= \left[F_{\mathrm{i}j}^{i}, A_j^i, E_{\mathrm{i}j}^{i}, S_j^i\right] \\ &(i = 1, 2, \ldots, n; j \in \{\min, \max, \mathrm{m}, \mathrm{var}\}), \end{aligned} \tag{12}$$

where F_i is the instantaneous frequency; A is the amplitude; E_i is the Hilbert instantaneous energy; S is the entropy; n is the number of BIMFS and the residue, with a value of 4 in this study; and min, max, m and var are short for minimum, maximum mean number and variance, respectively. Therefore, 64 dimension features are obtained in the initialization feature space. The feature extraction aims at finding an optimal feature subset. Fifty-seven dimension features remained because seven dimension features possess the same zero value. The relief algorithm is a well-known

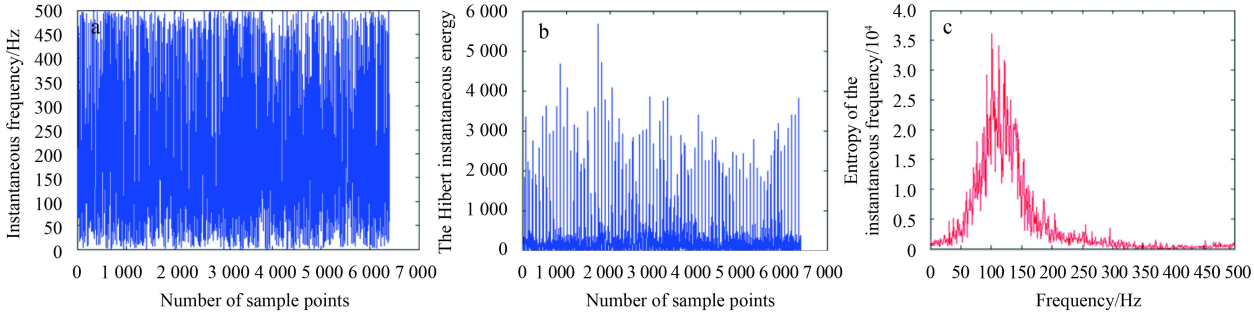

Fig. 6. HSA of Mode 1 for Fig. 4b. a. Instantaneous frequency diagram, b. Hilbert instantaneous energy diagram, and c. entropy of the instantaneous frequency diagram.

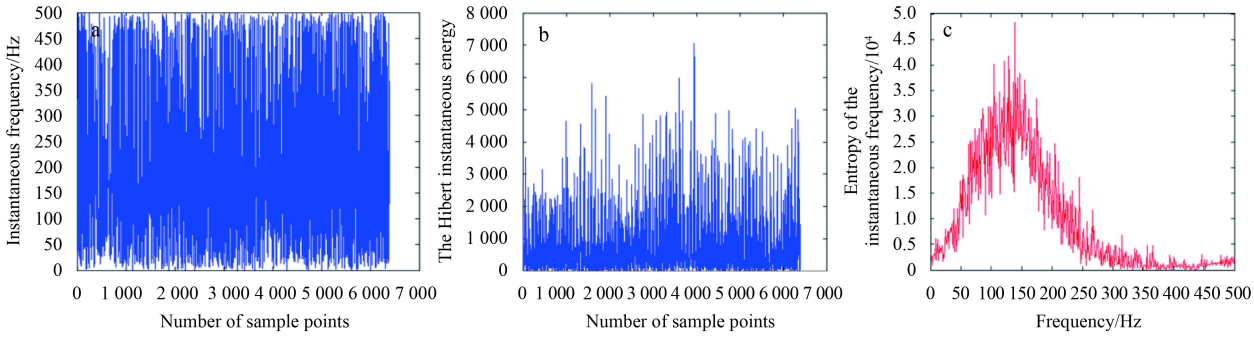

Fig. 7. HSA of Mode 1 for Fig. 4c. a. Instantaneous frequency diagram, b. Hilbert instantaneous energy diagram, and c. entropy of the instantaneous frequency diagram.

method that is developed by Kira and Rendell (1992) and is adapted to two-class problems. A total of 100 oil spill dark patches and 100 lookalikes dark patches are treated as samples. Relief can calculate a weight value to each feature, as shown in Fig. 8a. The weights can be divided into m parts, and get the partitioned histogram of weight as shown in Fig. 8b. m depends on the number of two classes of samples, which can be computed by

$$m = \text{round}[1.87(s_1 + s_2 - 1)^{0.4}] + 1, \tag{13}$$

where s_1 is the number of the first set of samples and s_2 is the number of the second set of samples.

Here m=17. The right weight value of sharp jump part that has the biggest difference between the adjacent parts is considered as a threshold in this paper, and the features valued over the threshold are selected. The threshold value of weight is 2.272 5 ×10^3 marked in triangle in Fig. 8b.

Finally, redundant features are deleted using a correlation analysis. Calculate the correlation coefficient matrix. Set the threshold value of correlation coefficient. Usually if the correlation coefficient is greater than 0.8, the two variables have a strong correlation. Small weights were removed in a pair of strong correlation features. The selected features are shown in Table 1. In Fig. 9, the selected features from our data set are reported. The dotted line and the solid line are an obvious difference. The figure shows that oil spills and look-alikes exhibit evident difference. The choice of parameters used to differentiate between oil spills and quasi-oil spills is feasible.

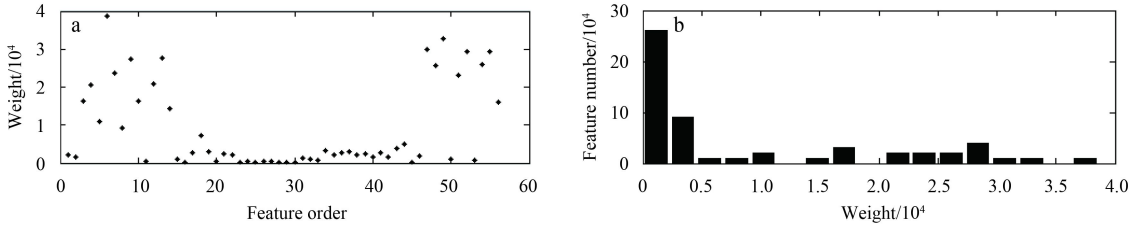

Fig. 8. Scatter diagram of weight value to each feature (a) and partitioned histogram of weight value (b).

Table 1. Selected features

Threshold value of weight	Threshold value of correlation coefficient	Selected features
2.272 5×10^3	0.8	F^3_{im}, E^4_{im}, $S^4_{\max}$, S^4_m, S^4_{var}

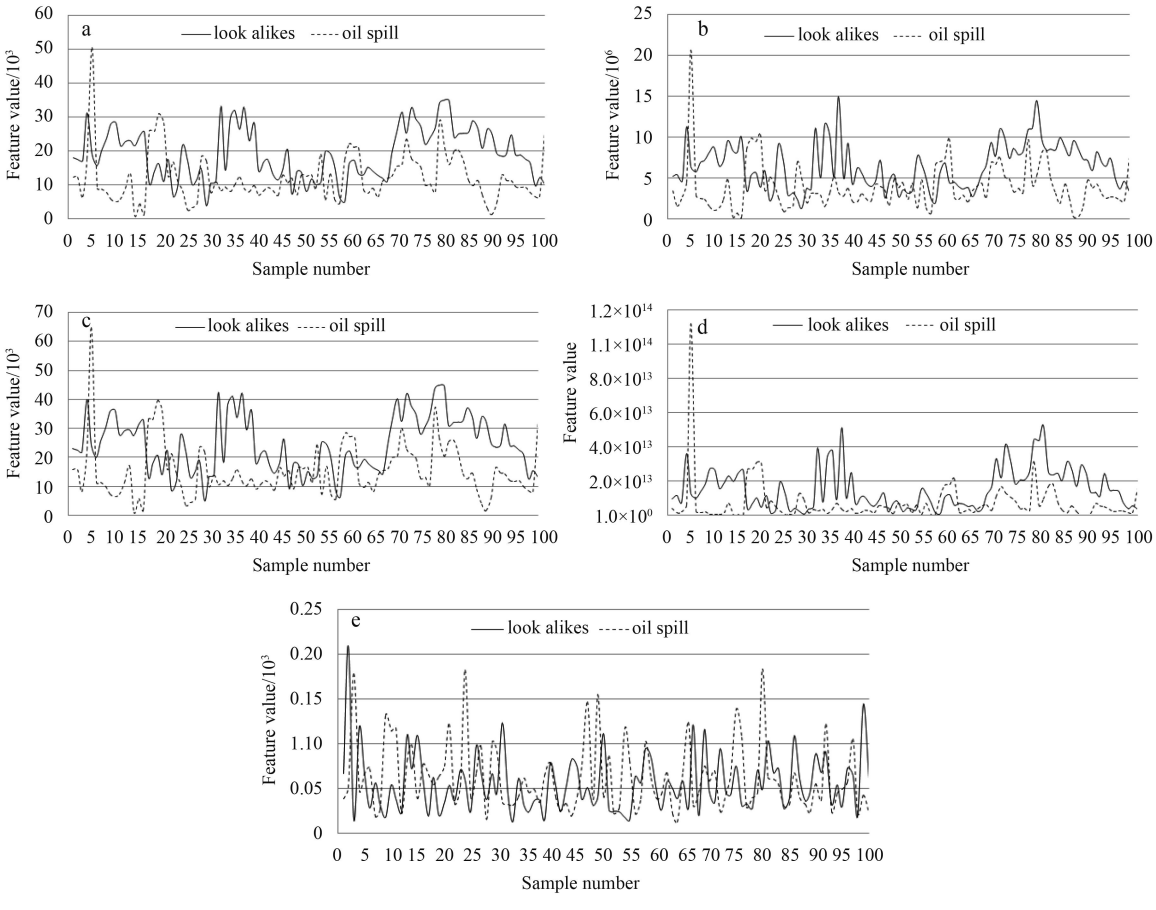

Fig. 9. Comparison of feature values about oil spills and look-alikes. a. E^4_{im}, b. $S^4_{\max}$, c. S^4_{m}, d. S^4_{var} and e. F^3_{im}.

4 Experimental validation

To evaluate the performance and feasibility of the proposed features in this paper, we generated two sets of samples, namely, oil spill and look-alikes. A kind of classifier is used to predict the category for each sample. The Mahalanobis distance is widely used in a cluster analysis and classification technologies. This paper used the Mahalanobis distance as a classifier and the algorithm as follows:

Step 1. Calculate the feature selected above vector $\bar{X}$ for each sample:

$$\begin{aligned}\bar{X} &= [X_1, X_2, X_3, X_4, X_5] \\ &= \left[F_{\text{im}}^3, E_{\text{im}}^4, S_{\max}^4, S_{\text{m}}^4, S_{\text{var}}^4\right],\end{aligned}$$

Step 2. Calculate the covariance matrix $\boldsymbol{C}$ to feature vector $\bar{X}$:

$$\begin{aligned}\boldsymbol{C} &= \boldsymbol{E}\left[(x-\boldsymbol{E}(x))\left(x-\boldsymbol{E}(x)^{\mathrm{T}}\right)\right] \\ &= \begin{bmatrix} E_{11} & E_{12} & \cdots & E_{1n} \\ E_{21} & E_{22} & \cdots & E_{2n} \\ \vdots & \vdots & & \vdots \\ E_{n1} & E_{n2} & \cdots & E_{nn} \end{bmatrix}.\end{aligned} \tag{14}$$

where $E_{11}=E[(x_1-u_1)(x_1-u_1)]$, $E_{12}=E[(x_1-u_1)(x_2-u_2)]$, $E_{1n}=E[(x_1-u_1)(x_n-u_n)]$, $E_{21}=E[(x_2-u_2)(x_1-u_1)]$, $E_{22}=E[(x_2-u_2)(x_2-u_2)]$, $E_{2n}=E[(x_2-u_2)(x_n-u_n)]$, $E_{n1}=E[(x_n-u_n)(x_1-u_1)]$, $E_{n2}=E[(x_n-u_n)(x_2-u_2)]$ and $E_{nn}=E[(x_n-u_n)(x_n-u_n)]$, u_i is the expectation value of the ith feature, $u_i=E(x_i)$.

Step 3. To use the Mahalanobis distance to classify a test point as belonging to one of two classes, we first compute the mean vector $\overline{M}_j^i (j=1,2)$ of samples known to belong to each class. This paper uses a training set as mentioned in Section 3.4. $\overline{M}_j^i$ is shown as below:

$$\begin{aligned}\overline{M}_1^i &= \{0.62\times10^{-1}, 1.21\times10^4, 3.93\times10^7, \\ &\quad 1.55\times10^5, 7.04\times10^{12}\}, \\ \overline{M}_2^i &= \{0.56\times10^{-1}, 1.91\times10^4, 6.42\times10^7, \\ &\quad 2.45\times10^5, 1.52\times10^{13}\}.\end{aligned} \tag{15}$$

Step 4. Compute the Mahalanobis distance r_j to each class by

$$r_j^2 = \left(\boldsymbol{X}-\overline{M}_j^i\right)^{\mathrm{T}} \boldsymbol{C}^{(-1)} \left(\boldsymbol{X}-\overline{M}_j^i\right) \quad (j=1,2) \tag{16}$$

and classify the test sample as belonging to the class with minimal Mahalanobis distance. If r_1 is less than r_2, the test sample is the image of oil film; otherwise, the image is a look-alike.

A dataset of 100 samples was selected as a test data set for classification. The top 50 samples are oil spill images, whereas the remaining number belongs to the class of look-alikes. The Mahalanobis distance of each sample is shown in Fig. 10. As shown in the figure, 45 samples possess r_1 that is less than r_2 in the top 50, and 46 samples possess r_2 that is less than r_1 in the remaining 50. The right is 45 oil spills and 46 look-alikes. Therefore, the overall accuracy is 91%. And once the ROIs (80×80) have been selected, the classification step needs about less than 1 second to complete their actions.

5 Evaluation of contributions

The paper compared the proposed method with a typical method on several data sets to evaluate its performance. A typical approach for oil spill detection involves locating dark areas in the SAR image and then computing texture and shape features for dark segments to define whether the target is an oil slick or something else. The first step is to segment out oil spill candidates as selected by a local threshold method. The threshold value corresponds to the local minimum between the two peaks in the histogram. Second, the features are extracted from previous studies, as shown in Table 2. The described set of features extracted from the dark object is inputted to a Mahalanobis distance classifier, which estimates the probability of being an oil slick or a look-alike. Different methods were tested in the same data set. Table 3 shows a comparison of the proposed method with a typical method.

6 Conclusions

A new algorithm is proposed for detecting oil spill from the SAR image based on Hilbert spectrum of the BEMD. Regions of interest in the SAR image are obtained by a histogram analysis. Each dark path is decomposed by the BEMD, and its Hilbert spectrum and Hilbert marginal spectrum are calculated. Afterward, the features are extracted by a relief algorithm. To demonstrate the validation, we divided different data sets into two categories, which are used to test the accuracy rate of the proposed method by the Mahalanobis distance. The accuracy of the classification increased. On the basis of the above results, the feature analysis of dark formations that are proposed in this paper is feasible. This method can effectively detect oil spills from the SAR image.

Although the BEMD method is based on the data itself, thus presenting good adaptability, several aspects remain to be investigated with regard to the BEMD, including the end effect, the interpolation method, parametric forms, and normalization processing. In addition, more intelligent algorithms (the neural net-

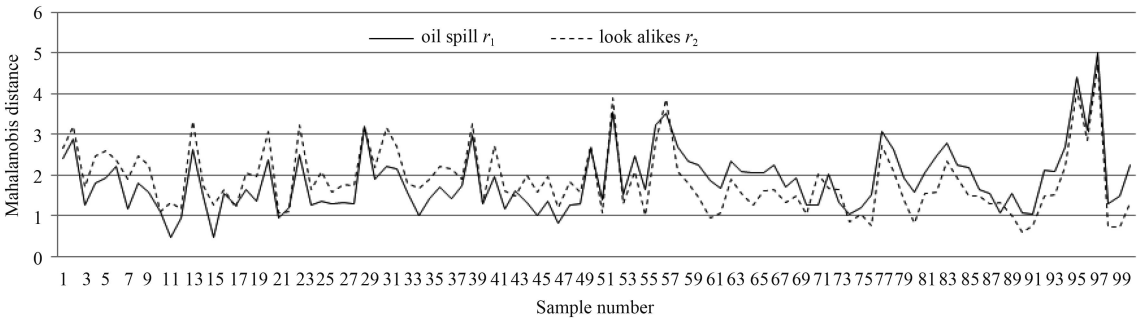

Fig. 10. Mahalanobis distance of every sample.

Table 2. Selected features in previous studies

No.	Features	Frate et al. (2000)	Zhang et al. (2008)	Guo and Zhang (2014)
1	slick area	√		
2	slick perimeter	√		
3	slick complexity	√		√
4	marking ratio			√
5	solidity			√
6	rectangular saturation			√
7	spreading (low for long thin slicks, high for circular shape)	√		√
8	edge density			√
9	interior angles based on bounding polygons			√
10	object standard deviation	√		
11	background standard deviation	√		
12	max contrast (between object and background)	√		
13	mean contrast (between object and background)	√		
14	max border gradient	√		
15	mean border gradient	√		
16	gradient standard deviation	√		
17	hu moment invariant			√
18	elliptical Fourier descriptors			√
19	co-occurrence textural features (mean, variance, homogeneity, contrast, dissimilarity)		√	

Table 3. Comparison of the proposed method with a typical method

Method	Overall accuracy		
	Data set A (50 oil spills, 50 look-alikes)/%	Data set B (58 oil spills, 142 look-alikes)/%	Data set C (133 oil spills, 67 look-alikes)/%
Frate et al. (2000)	90	84	87
Zhang et al. (2008)	89	86	85
Guo and Zhang (2014)	92	91	89
Proposed method	91	92	90

work, fuzzy clustering, etc.) and data sets (Radarsat-2, ship-borne radar, shore-base radar, etc.) will be used to verify the validation of the proposed method in the future.

References

Bern T I, Wahl T, Andersen T, et al. 1993. Oil spill detection using satellite based SAR: experience from a field experiment. Photogrammetric Engineering and Remote Sensing, 59(3): 423–428

Brekke C, Solberg A H S. 2005. Oil spill detection by satellite remote sensing. Remote Sensing of Environment, 95(1): 1–13

Chaudhuri D, Samal A, Agrawal A, et al. 2012. A statistical approach for automatic detection of ocean disturbance features from SAR images. IEEE Journal of Selected Topics in Applied Earth Observations and Remote Sensing, 5(4): 1231–1242

Chen Lu, Li Xiuxiu, Lin Yimao, et al. 2012. Texture classification based on feature extraction with BEMD and LBP. Computer Applications and Software (in Chinese), 29(9): 243–245

Chen Zhong, Luo Song, Xie Ting, et al. 2014. A novel infrared small target detection method based on BEMD and local inverse entropy. Infrared Physics & Technology, 66: 114–124

Cheng Yongcun, Li Xiaofeng, Xu Qing, et al. 2011. SAR observation and model tracking of an oil spill event in coastal waters. Marine Pollution Bulletin, 62(2): 350–363

Dong Shiwei, Zhou Ziyong, Wen Baihong. 2010. Feature extraction of offshore oil slick from hyperspectral data based on EMD and neural network. Remote Sensing Technology and Application, 25(2): 221–226

Frate F D, Petrocchi A, Lichtenegger J, et al. 2000. Neural networks for oil spill detection using ERS-SAR data. IEEE Transactions on Geoscience and Remote Sensing, 38(5): 2282–2287

Guo Yue, Zhang Hengzhen. 2014. Oil spill detection using synthetic aperture radar images and feature selection in shape space. International Journal of Applied Earth Observation and Geoinformation, 30: 146–157

He Zhi, Wang Qiang, Shen Yi, et al. 2013. Multivariate gray model-based BEMD for hyperspectral image classification. IEEE Transactions on Instrumentation and Measurement, 62(5): 889–904

Kira K, Rendell L A. 1992. The feature selection problem: traditional methods and a new algorithm. Tenth National Conference on Artificial Intelligence. California: AAAI Press, 129–134

Liu Zhongxuan, Peng Silong. 2005. Directional EMD and its application to texture segmentation. Science in China Series: F. Information Sciences, 48(3): 354–365

Marghany M. 2015. Automatic detection of oil spills in the Gulf of Mexico from RADARSAT-2 SAR satellite data. Environmental Earth Sciences, 74(7): 5935–5947

Nirchio F, Sorgente M, Giancaspro A, et al. 2005. Automatic detection of oil spills from SAR images. International Journal of Remote Sensing, 26(6): 1157–1174

Nunes J C, Bouaoune Y, Delechelle E, et al. 2003. Image analysis by bidimensional empirical mode decomposition. Image and Vision Computing, 21(12): 1019–1026

Nunes J C, Guyot S, Deléchelle E. 2005. Texture analysis based on local analysis of the bidimensional empirical mode decomposition. Machine Vision and Applications, 16(3): 177–188

Nunziata F, Migliaccio M, Gambardella A. 2011. Pedestal height for sea oil slick observation. IET Radar, Sonar & Navigation, 5(2): 103–110

Pavlakis P, Sieber A J, Alexandry S. 1996. Monitoring oil-spill pollution in the Mediterranean with ERS SAR. ESA Earth Observation Quarterly, 52: 1–6

Salberg A B, Rudjord O, Solberg A H S. 2014. Oil spill detection in hybrid-polarimetric SAR images. IEEE Transactions on

Geoscience and Remote Sensing, 52(10): 6521–6533

Skrunes S, Brekke C, Eltoft T. 2014. Characterization of marine surface slicks by Radarsat-2 multipolarization features. IEEE Transactions on Geoscience and Remote Sensing, 52(9): 5302–5319

Solberg A H S. 2012. Remote sensing of ocean oil-spill pollution. Proceedings of the IEEE, 100(10): 2931–2945

Topouzelis K N. 2008. Oil spill detection by SAR images: dark formation detection, feature extraction and classification algorithms. Sensors, 8(10): 6642–6659

Zhang Fengli, Shao Yun, Tian Wei, et al. 2008. Oil spill identification based on textural information of SAR image. IEEE Geoscience and Remote Sensing Symposium, 5: 1308–1311

Zheng Quanan, Zhao Qing, Nan W, et al. 2010. Oil spill in the Gulf of Mexico and spiral vortex. Acta Oceanologica Sinica, 29(4): 1–2